

Supporting Information

Modifying the quality factors of the bound states in the continuum in a dielectric metasurface by mode coupling

Zhaotang Li,^{1#} Lidan Zhou,^{1,2#} Zhuojun Liu,^{3} Mingcheng Panmai,¹ Shulei Li,^{1,4} Jin Liu,⁵ and Sheng Lan^{1*}*

1. Guangdong Provincial Key Laboratory of Nanophotonic Functional Materials and Devices, School of Information and Optoelectronic Science and Engineering, South China Normal University, Guangzhou 510006, China.

2. State Key Laboratory of Optoelectronic Materials and Technologies, School of Electronics and Information Technology, Sun Yat-sen University, Guangzhou 51006, China.

3. State Key Laboratory for Mesoscopic Physics and Frontiers Science Center for Nano-optoelectronics, School of Physics, Peking University, Beijing 100871, China

4. School of Optoelectronic Engineering, Guangdong Polytechnic Normal University, Guangzhou 510665, China

5. State Key Laboratory of Optoelectronic Materials and Technologies, School of Physics, Sun Yat-sen University, Guangzhou 510275, China

These authors contributed equally to this work.

*Corresponding author: Zhuojun Liu zhuojunliu@pku.edu.cn; Sheng Lan slan@scnu.edu.cn

Supplementary Note 1: Multipolar expansion analysis

In order to find out the physical origin for the quasi-BIC supported by a metasurface, we performed multipolar expansion analysis for the quasi-BIC based on the following formulas. We first calculated the current density from the electric field by using the following equation:

$$\vec{J} = -i\omega(\varepsilon-1)\vec{E}(\vec{r}). \quad (1)$$

Here, ω is the frequency of the incident wave and ε is the dielectric constant of the material. Then, the electric dipole moment \vec{p} , the magnetic dipole moment \vec{m} , the toroidal dipole moment \vec{T} , the electric quadrupole moment EQ , and the magnetic quadrupole moment MQ could be derived as follows¹:

$$\vec{p} = \frac{1}{i\omega} \int \vec{J}(\vec{r}) d^3r \quad (2)$$

$$\vec{m} = \frac{1}{2c} \int \vec{r} \times \vec{J}(\vec{r}) d^3r \quad (3)$$

$$\vec{T} = \frac{1}{10c} \int \{[\vec{r} \cdot \vec{J}(\vec{r})]\vec{r} - 2(\vec{r} \cdot \vec{r})\vec{J}(\vec{r})\} d^3r \quad (4)$$

$$EQ_{\alpha\beta} = \frac{1}{2i\omega} \int \{r_{\alpha} J_{\beta}(\vec{r}) + r_{\beta} J_{\alpha}(\vec{r}) - \frac{2}{3}[\vec{r} \cdot \vec{J}(\vec{r})]\delta_{\alpha\beta}\} d^3r \quad (5)$$

$$MQ_{\alpha\beta} = \frac{1}{3c} \int \{[\vec{r} \times \vec{J}(\vec{r})]_{\alpha} r_{\beta} + [\vec{r} \times \vec{J}(\vec{r})]_{\beta} r_{\alpha}\} d^3r \quad (6)$$

Finally, the corresponding far-field radiation powers of \vec{p} , \vec{m} , \vec{T} , EQ , and MQ can be obtained by using the following equations:

$$I_p = \frac{\mu_0 \omega^4}{12\pi c} |\vec{p}|^2, I_m = \frac{\mu_0 \omega^4}{12\pi c} |\vec{m}|^2, I_T = \frac{\mu_0 \omega^4 k^2}{12\pi c} |\vec{T}|^2, I_{EQ} = \frac{\mu_0 \omega^4 k^2}{40\pi c} \sum |EQ_{\alpha\beta}|^2, I_{MQ} = \frac{\mu_0 \omega^4 k^2}{160\pi c} \sum |MQ_{\alpha\beta}|^2. \quad (7)$$

For the reconstruction of the reflection or transmission spectra of quasi-BICs, two modified terms must be considered¹:

$$\vec{T}^{(1)} = \frac{1}{28c} \int \{3[(\vec{r} \cdot \vec{r})\vec{J}(\vec{r})] - 2[\vec{r} \cdot \vec{J}(\vec{r})]\vec{r}\}(\vec{r} \cdot \vec{r}) d^3r \quad (8)$$

$$\vec{m}^{(1)} = \frac{1}{2c} \int [\vec{r} \times \vec{J}(\vec{r})](\vec{r} \cdot \vec{r}) d^3r \quad (9)$$

Then, the reflection coefficient can be expressed as¹:

$$r = \frac{\mu_0}{2\Delta E_0} \{-ikP_{\parallel} + ik\hat{R} \times (M_{\parallel} - \frac{k^2}{10}M_{\parallel}^{(1)}) - k^2(T_{\parallel} + \frac{k^2}{10}T_{\parallel}^{(1)}) + k^2(EQ \cdot \hat{R})_{\parallel} - \frac{k^2}{2}\hat{R} \times (MQ \cdot \hat{R})_{\parallel}\}. \quad (10)$$

Here, E_0 is the electric field intensity of the incident wave, \parallel denotes the x or y component, Δ denotes the area of one unit cell, $\hat{k} = \mathbf{k}/k$ indicates the direction of the incident plane wave, and $\hat{R} = -\hat{k}$.

For lossless materials, the transmission can be extracted from the reflection coefficient as follows:

$$T = 1 - |r|^2 \quad (11)$$

Supplementary Note 2: Dependence of the Q factor of the quasi-BIC on the scaling factor

In Figure S1, we show the dependence of the Q factor of the quasi-BIC on the scaling factor s calculated for metasurfaces with structural parameters $p_x = p_y = 720$ nm, $h = 500$ nm, $w = 400 \times s$ nm, $a = 160 \times s$ nm, $b = 60 \times s$ nm and different scaling factors. It can be seen that the resonant wavelength of the quasi-BIC can be continuously tuned from ~ 1330 to ~ 1750 nm. Meanwhile, it is noticed that the Q factor of the quasi-BIC decreases monotonously from $\sim 1.4 \times 10^5$ to $\sim 3 \times 10^4$ as s is increased from 0.8 to 1.2. The largest Q factor is not observed for $s = 1.0$ where the quasi-BIC exhibits a symmetric Lorentz lineshape in the transmission spectrum (see Figure 1c in the main text).

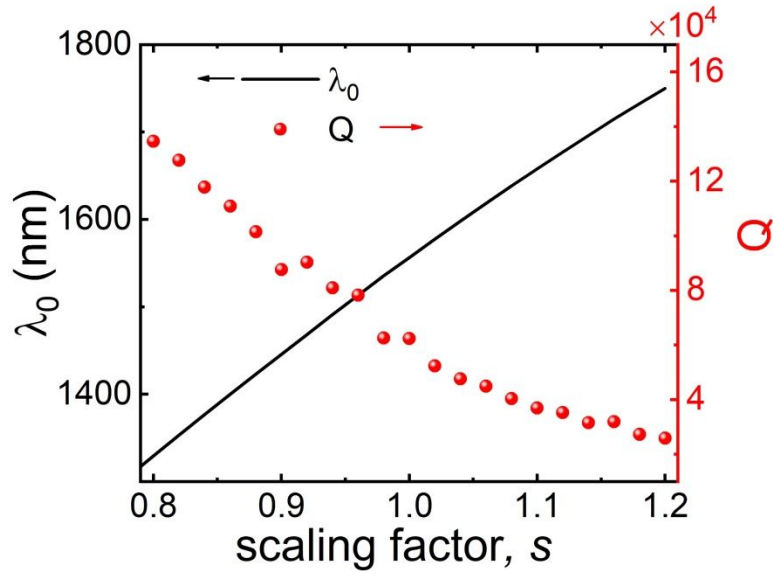


Figure S1. Dependence of the Q factor of the quasi-BIC on the scaling factor s calculated for metasurfaces with structural parameters $p_x = p_y = 720$ nm, $h = 500$ nm, $w = 400 \times s$ nm, $a = 160 \times s$ nm, $b = 60 \times s$ nm (see also Figure 1c in the main text).

Supplementary Note 3:

In Figure 2a, five quasi-BICs are revealed in the transmission spectrum of the metasurface in the wavelength range of 1200-1800 nm. It is noticed that mode ⑤ appears as a Fano peak while modes ①–④ appear as Fano dips. In Figure S2a,b,c,d,e, we present the transmission spectra and multipolar expansion analyses for the five quasi-BICs. In each case, the electric and magnetic field distributions in the Si cuboid are shown as the insets. It can be seen that mode ① is formed by the interference between ED_y and MQ_{xz} (magnetic quadrupole in the xz plane), which leads to the directional radiation in the x direction. Mode ② is governed by MQ_{xy} (magnetic quadrupole in the xy plane), which is manifested clearly in the electric and magnetic field distributions. Its radiation appears as four lobes in the xy plane. Mode ③ is dominated by a ED oriented in the z direction (i.e., ED_z), giving rise to a doughnut-shaped radiation pattern. Interestingly, mode ④ is governed by MQ_{zz} , which is composed of two out-of-phase MDs oriented in the z direction (i.e., MD_z). A clockwise circular electric field distribution is observed in the the upper part of the Si cuboid while an anti-clockwise circular one is found in the lower part, resulting in a diabolo-like radiation pattern. Mode ⑤ has been widely studied in literature. It is dominated by MD_z with a doughnut-shaped radiation pattern and a dark axis in the z direction. Based on the above analysis, it is found that the quasi-BICs are governed by optical modes radiate in the xy direction (e.g., modes ②–⑤) or created by the destructive interference of two optical modes (e.g., mode ①).

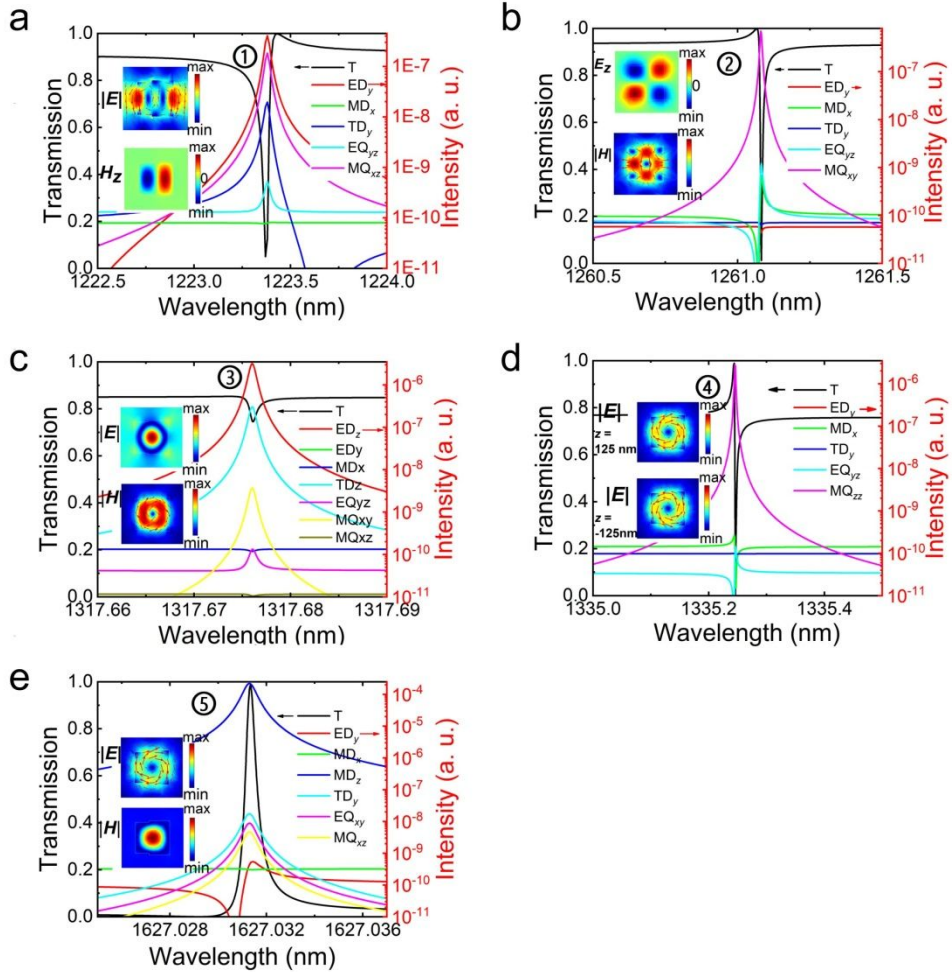


Figure S2. (a),(b),(c),(d),(e) Transmission spectra and multipolar expansion analyses for the five quasi-BICs shown in Figure 2. In each case, the electric and magnetic field distributions in the Si cuboid are provided as the insets.

Supplementary Note 4: Reconstructed transmission spectra for the quasi-BICs based on the multipole decomposition method

Relying on the multiple decomposition method (see Supplementary Note 1), we could reconstructed the transmission spectra of the quasi-BICs. Some examples are shown in Figure S3, where the reconstructed transmission spectra of two quasi-BICs (modes ④ and ⑤) are compared with those obtained directly based on the numerical simulation. It can be seen that in both cases the reconstructed transmission spectra are in good agreement with the simulation results.

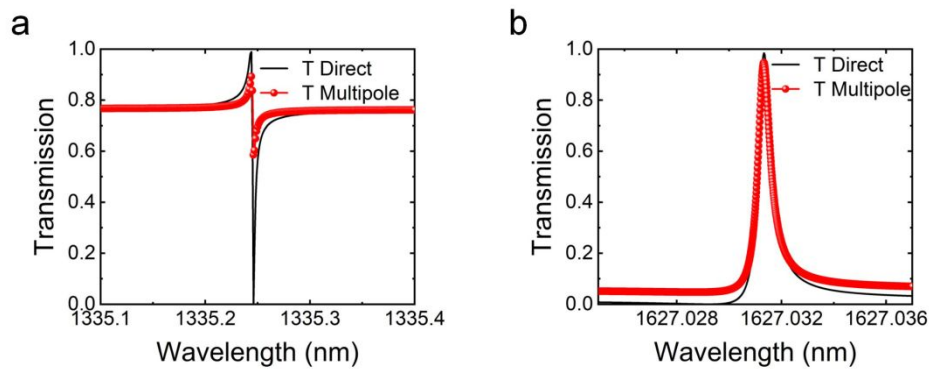


Figure S3. Comparison of the transmission spectrum reconstructed by using the multipole decomposition method and that obtained by numerical simulation. (a) Mode ④. (b) Mode ⑤.

Supplementary Note 5: Optical properties of the quasi-BICs supported by the metasurface with defect

As discussed in the main text, we observed five quasi-BICs in the transmission spectrum of the metasurface with defect ($p_x = 720$ nm, $p_y = 700$ nm, $w = 400$ nm, $h = 500$ nm, $a = 160$ nm, $b = 20$ nm) in the spectral range of 1200–1800 nm. The optical properties of these quasi-BICs, including their resonant wavelengths, Q factors, and enhancement factors for electric and magnetic fields, are summarized in Table S1. The integration runs over the volume of the Si cuboid.

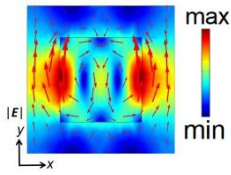
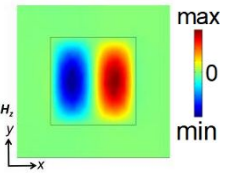
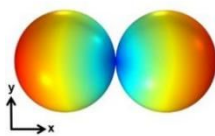
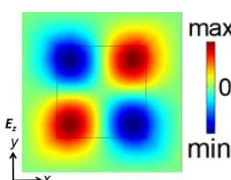
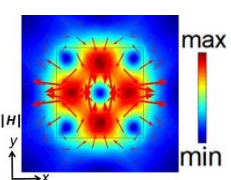
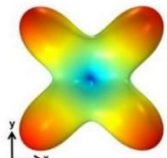
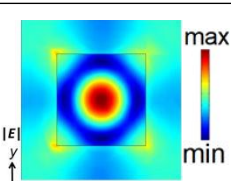
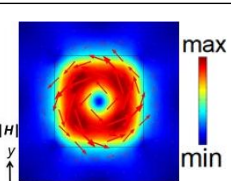
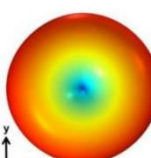
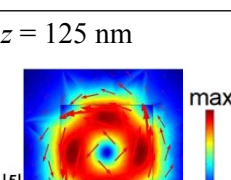
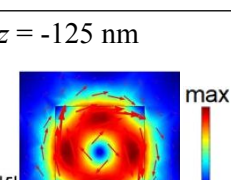
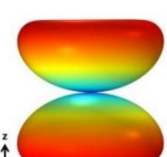
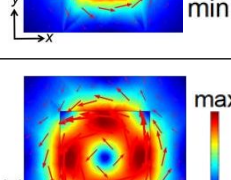
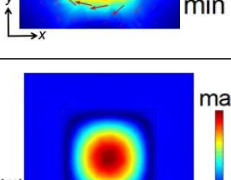
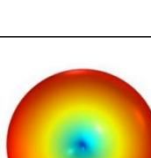
Table S1. Resonant wavelengths, Q factors, and enhancement factors for electric and magnetic fields of the quasi-BICs supported by the metasurface with defect

λ_0 (nm)	Q	$\frac{1}{V} \int E /E_0 dV$	$\frac{1}{V} \int H /H_0 dV$
1223.37	4.1e4	59.9	186.5
1261.082	1.86e5	140.5	382.1
1317.6762	2e6	86.6	313.7
1335.246	6.58e5	271	760.5
1627.0313	2.89e6	804.2	2031.5

Supplementary Note 6: Physical origins for the quasi-BICs supported by the metasurface without defect

As discussed in the main text, we observed five quasi-BICs in the transmission spectrum of the metasurface without defect ($p_x = 720$ nm, $p_y = 700$ nm, $w = 400$ nm, $h = 500$ nm) in the spectral range of 1200–1900 nm (see Figure 3a). In Table S2, we present the electric and magnetic field distributions in the xy plane calculated for the quasi-BICs. In addition, we also examine the far-field radiation patterns of the quasi-BICs in the xy plane (except mode ④ in the xz plane).

Table S2 Electric and magnetic field distributions and radiation patterns of the quasi-BICs supported by the metasurfaces without defect

① ED_y MQ_{xz}			
② MQ_{xy}			
③ ED_z			
④ MQ_{zz}	$z = 125$ nm 	$z = -125$ nm 	
⑤ MD_z			

Supplementary Note 7: Optical properties of the quasi-BICs supported by the metasurface without defect

As discussed in the main text, we observed five quasi-BICs in the transmission spectrum of the metasurface without defect ($p_x = 720$ nm, $p_y = 700$ nm, $w = 400$ nm, $h = 500$ nm) in the spectral range of 1200–1900 nm. The optical properties of the quasi-BICs, including their resonant wavelengths, Q factors, and enhancement factors for electric and magnetic fields, are summarized in Table S3. The integration runs over the volume of the Si cuboid.

Table S3. Resonant wavelengths, Q factors, and enhancement factors for electric and magnetic fields of the quasi-BICs supported by the metasurfaces without defect

	λ_0 (nm)	Q	$\frac{1}{V} \int E / E_0 dV$	$\frac{1}{V} \int H / H_0 dV$
①	1234.269	5.2e4	75	215
②	1285.1475	3.7e6	777	1932.3
③	1334.09993	5e7	535.8	1771
④	1349.725408	2.6e8	7135.1	18391.2
⑤	1649.6172359	4.87e8	2.8e4	1.24e5

Supplementary Note 8: Configurations of metasurfaces composed of Si cylinders and spheres

In Figure S4 a,b, we show schematically the configurations of the metasurfaces composed of periodically arranged Si cylinders and spheres, respectively.

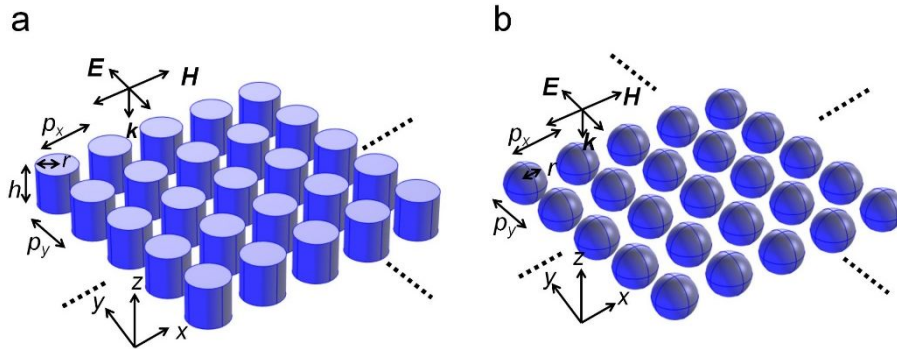


Figure S4. Schematics showing the configurations of the metasurfaces composed of periodically arranged Si cylinders (a) and spheres (b). The periods in the x and y directions are p_x and p_y . The plane wave is incident from the $-z$ direction with its electric and magnetic fields along the y and x directions.

Supplementary Note 9

In Figure S5a,b, we show the spectral lineshapes of two quasi-BICs revealed in the transmission spectra of a metasurface composed of Si cylinders with a diameter of $d = 440$ nm and a height of $h = 500$ nm. The periods of the metasurface were set to be $p_x = p_y = 720$ nm. The electric/magnetic field distributions are shown in the insets. In this case, the quasi-BIC located at 1238.538 nm possesses a Q factor of 3.0×10^5 . It arises from the interference of ED_y and MQ_{xz} . Another quasi-BIC appears at 1671.724 nm and possesses a much higher Q factor of 2.09×10^8 . This quasi-BIC is governed by MD_z . In Figure S5c,d, we present the spectral lineshapes of the two quasi-BICs revealed in the transmission spectra of a metasurface composed of Si spheres with a diameter of $d = 500$ nm. The periods of the metasurface were set to be $p_x = p_y = 720$ nm. Also shown are the multipolar expansion analysis for the two modes. While the quasi-BIC at the short wavelength ($\lambda = 1278$ nm) is created by the interference of ED_y and MQ_{xz} , the quasi-BIC at the long wavelength ($\lambda = 1670.267566$ nm, $Q = 2.68 \times 10^8$) is dominated by MD_z . These two quasi-BICs correspond to the modes ① and ⑤ revealed in the metasurface composed of Si cuboids.

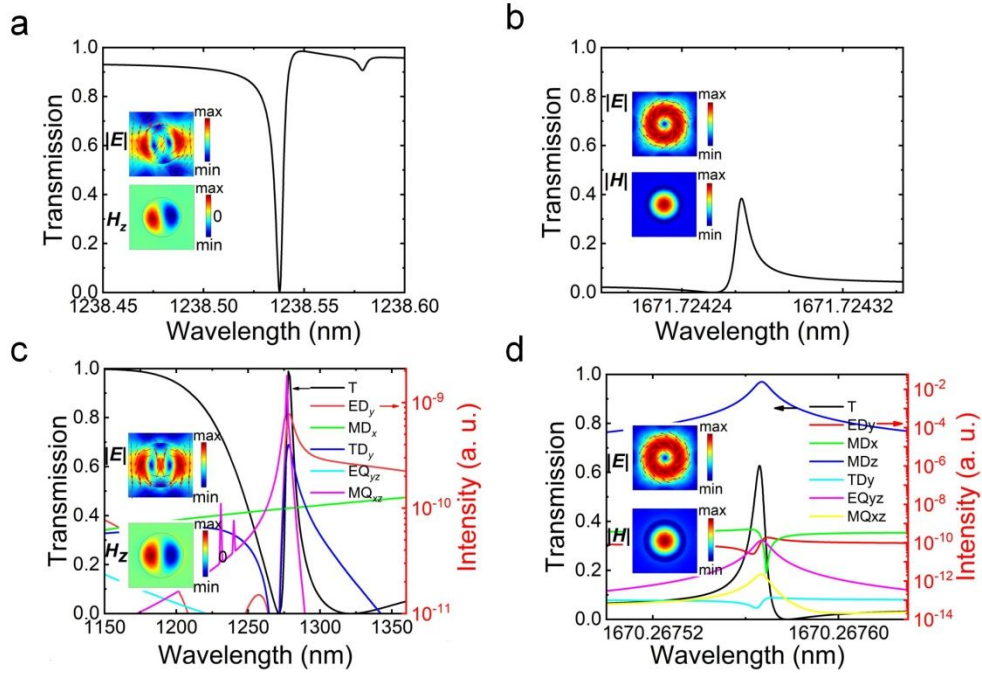


Figure S5. (a) and (b) Transmission spectrum calculated for the metasurface with cylinders structure corresponding to mode ① and ⑤, respectively. (c) and (d) Transmission spectrum and multipolar expansion calculated for the metasurface with spheres structure corresponding to mode ① and ⑤, respectively. The electric and magnetic field distributions in a Si cylinders or spheres are shown as insets.

Supplementary Note 10: Excitation of the quasi-BIC with dipole sources

As discussed in main text, one of the quasi-BICs of the metasurface (mode ⑤) is dominated by MD_z . The leakage of MD_z arises from the interference with ED_y/MD_x , leading to a Fano lineshape. In order to confirm this, we excited the metasurface ($p_x = p_y = 720$ nm, $h = 500$ nm, $w = 400 \times s$, $a = 160 \times s$, $b = 60 \times s$, $s = 0.8$, corresponding to Figure 3c in main text) with an electric dipole source oriented along the y direction (i.e., ED_y) or a magnetic dipole source oriented along the x direction (i.e., MD_x). In both cases, the electric/magnetic dipole source was placed at the center of the Si cuboid. In Figure S6 a,b, we show the optical modes excited in the Si cuboid by using ED_y and MD_x , respectively. In each case, the optical mode is decomposed into the contributions of Mie resonances of different orders. It can be seen that the optical mode is governed by MD_z in both cases, implying MD_z can be effectively excited either by ED_y or by MD_x due to the coupling between them. When the metasurface is excited by a plane wave propagating along the $-z$ direction, the quasi-BIC (MD_z) can be excited by the electric (ED_y) and magnetic (MD_x) components of the plane wave. In other words, the interaction between MD_z and ED_y/MD_x provides a channel for coupling the incident wave into the metasurface and the radiation of MD_z into the far field.

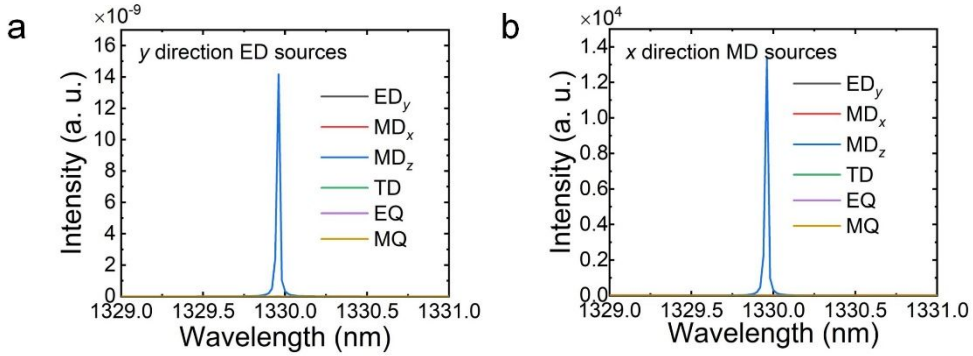


Figure S6. Optical modes excited in the metasurface ($p_x = p_y = 720$ nm, $h = 500$ nm, $w = 400 \times s$, $a = 160 \times s$, $b = 60 \times s$, $s = 0.8$) by using an electric (a) and a magnetic (b) dipole source placed at the center of the Si cuboid. In each case, the optical mode has been decomposed into Mie resonances of different orders.

Supplementary Note 11: Dependence of the resonant wavelength and Q factor of the quasi-BIC on the period

In Figure S7a, we show the dependence of the resonant wavelength of the quasi-BIC on the period in the y direction (p_y) calculated for metasurfaces with different defects characterized by b values. The solid circles indicate the wavelengths and periods at which the maximum Q factor is achieved. We also examined the dependence of the Q factor on the period in the x direction (p_x) for metasurfaces with different defects (i.e., different b values), as shown in Figure S7b. In Figure S7c, we show the dependence of the resonant wavelength of the quasi-BIC on the period (p_x) calculated for metasurfaces with different defects. The resonant wavelengths and periods at which the maximum Q factor is achieved are marked by solid circles. With increasing b , a decrease in p_x for maximum Q factor is observed. This behavior is different from what is observed in the dependence of the Q factor on p_y (see Figure S7a).

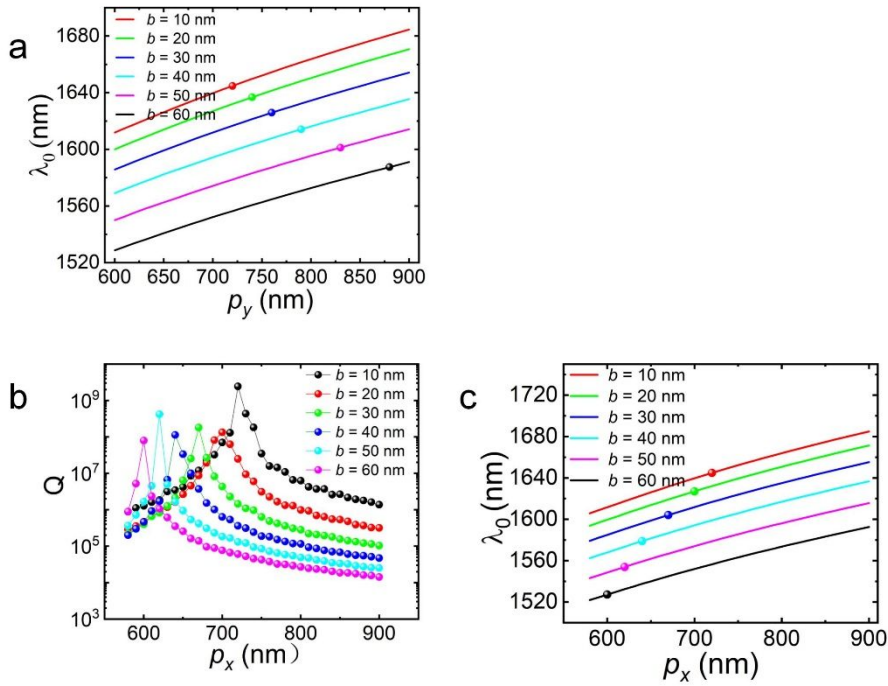


Figure S7. (a) Dependence of the resonant wavelength of the quasi-BIC on p_y calculated for metasurfaces with different defects (different b values). The solid circles indicate the resonant wavelengths and periods at which the maximum Q factor is achieved. (b) Dependence of the Q factor on p_x calculated for metasurfaces with different defects (different b values). (c) Dependence of the resonant wavelength of the quasi-BIC on p_x calculated for metasurfaces with different defects (different b values). The solid circles indicate the resonant wavelengths and periods at which the maximum Q factor is achieved.

Supplementary Note 12: Dependence of the Q factor of the quasi-BIC on defect size

We examined the dependence of the Q factor of the quasi-BIC on the structural parameter b , which characterizes the defect size of the Si cuboid, for metasurfaces with different configurations. In Figure S8a, we show the dependence of the Q factor of the quasi-BIC on the value of b for a metasurface with structural parameters $p_x = p_y = 720$ nm, $h = 500$ nm, $w = 400$ nm, $a = 160$ nm. It can be seen that the Q factor decreases exponentially with increasing b . This behavior is commonly observed in metasurfaces with defects. In Figure S8b, we present the relationship between the Q factor and the value of b for another metasurface with structural parameters $p_x = 720$ nm, $p_y = 842$ nm, $h = 500$ nm, $w = 400$ nm, $a = 160$ nm. Interestingly, it is remarkable that the Q factor first decreases and then increases exponentially with increasing b , reaching a maximum at $b = 50$ nm, and decreases exponentially with a further increase of b . This behavior is different from what we expect from general rule of symmetry breaking. It indicates clearly the important role of mode coupling, which is governed by the period, in determining the Q factor of the quasi-BIC.

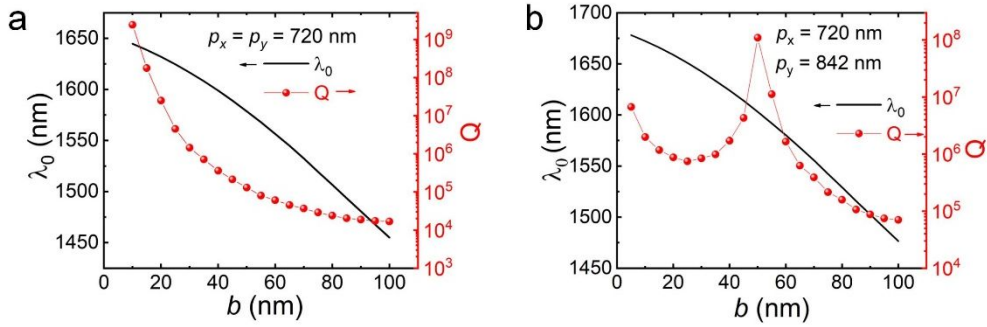


Figure S8. Dependence of the Q factor of the quasi-BIC on the value of b calculated for metasurfaces with structural parameters: (a) $p_x = p_y = 720$ nm, $h = 500$ nm, $w = 400$ nm, $a = 160$ nm; (b) $p_x = 720$ nm, $p_y = 842$ nm, $h = 500$ nm, $w = 400$ nm, $a = 160$ nm. In each case, the dependence of the resonant wavelength of the quasi-BIC on the value of b is also provided.

Supplementary Note 13: Radiation patterns at the quasi-BICs of the metasurfaces with different periods

As discussed in the main text, the Q factor of the quasi-BIC exhibits a strong dependence on the periods of the metasurface. Since the quasi-BIC originates from the interference between MD_z and ED_y/MD_x and the radiation of MD_z in the xy plane appears as a doughnut, it is expected that the difference in the Q factor should be reflected in the radiation pattern of the quasi-BIC. In Figure S9, we present the radiation patterns in the xy plane calculated for the quasi-BICs at different periods in the x direction (p_x). The other structural parameters of the metasurfaces are $p_y = 720$ nm, $h = 500$ nm, $w = 400$ nm, $a = 160$ nm, $b = 30$ nm. It can be seen that the radiations patterns for $p_x = 550$ nm and 1000 nm appear as ellipses with long axes along y and x directions, respectively. In contrast, a circular radiation pattern is observed for the quasi-BIC with $p_x = 670$ nm where the maximum Q factor is observed. In this case, the intensity of MD_z is much larger than that of ED_y/MD_x , leading to a negligible distortion of the radiation pattern.

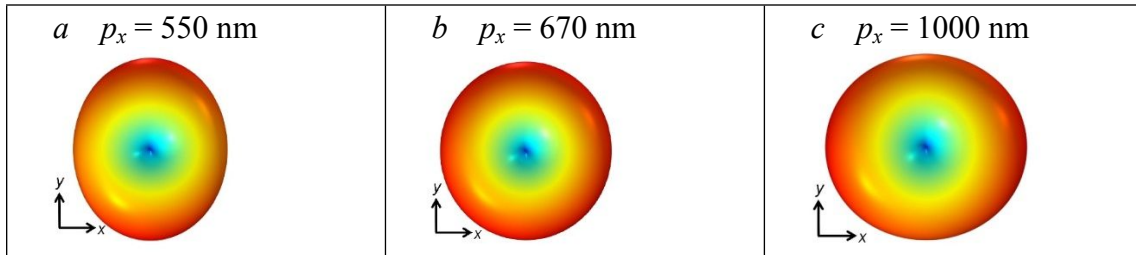


Figure S9. Radiation patterns at the quasi-BICs calculated for metasurfaces with different p_x . (a) $p_x = 550$ nm; (b) $p_x = 670$ nm; (c) $p_x = 1000$ nm. The other structural parameters of the metasurfaces are $p_y = 720$ nm, $h = 500$ nm, $w = 400$ nm, $a = 160$ nm, $b = 30$ nm.

Supplementary Note 14: Dependence of the field enhancement factor on the period

We examined the enhancement factors for the electric and magnetic fields for metasurfaces with different periods. In Figure S10a, we show the dependence of the enhancement factors on the period in the y direction (p_y) for a metasurface with $p_x = 720$ nm and $b = 30$ nm. The dependence of the Q factor on p_y is also provided. It can be seen that the enhancement factor exhibits a dependence on p_y quite similar to that of the Q factor. The largest enhancement factors are achieved at the p_y where the maximum Q factor is observed. In Figure S10b, we present the dependence of the enhancement factors on p_x calculated for another metasurface with $p_y = 720$ nm, $b = 50$ nm. In this case, a similar phenomenon is observed.

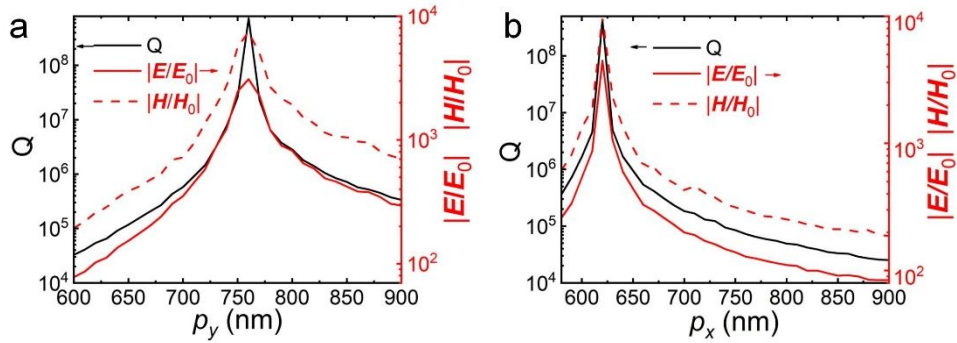


Figure S10. Dependence of the enhancement factors for electric and magnetic fields on the periods calculated for a metasurface with (a) $p_x = 720$ nm and $b = 30$ nm and (b) $p_y = 720$ nm, $b = 50$ nm. In each case, the dependence of the Q factor on the period is also provided for reference.

Supplementary Note 15: Comparison of the quasi-BICs for metasurfaces with different structures

In this work, we have examined the quasi-BICs supported in metasurfaces composed of elements with and without defects. In Figure S11, we compared the dependence of the Q factor on the period observed for the four metasurfaces discussed in the main text. The constituent elements include Si cuboid with defect ($w = 400$ nm, $h = 500$ nm, $a = 160$ nm, $b = 20$ nm), Si cuboid without defect ($w = 400$ nm, $h = 500$ nm), Si cylinder ($r = 220$ nm, $h = 500$ nm), and Si sphere ($r = 250$ nm). It is found that the Q factors of the quasi-BICs formed in the metasurfaces without defects are no longer sensitive to the period. The Q factors are distributed in the range of 10^{10} – 10^{13} with a small fluctuation. In contrast, the Q factor of the quasi-BIC achieved in the metasurface with defect exhibits a strong dependence on the period and the maximum value is close to that observed for the metasurfaces without defects.

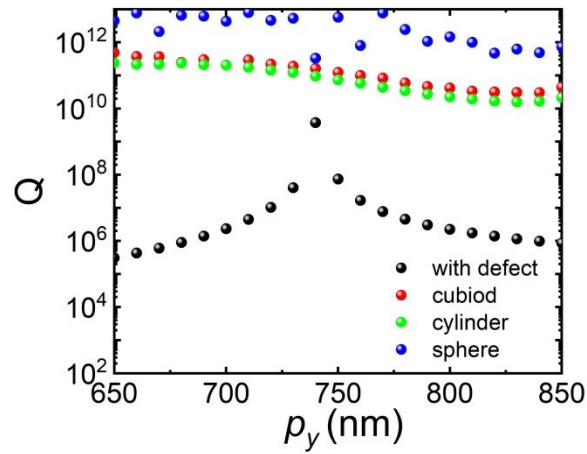


Figure S11. Dependence of the Q factor on the period p_y calculated for the four metasurfaces discussed in the main text.

Supplementary Note 16: Sample fabrication

A silicon-on-insulator (SOI) wafer (SOITEC) was used in the fabrication of metasurfaces composed of regularly arranged Si cuboids. It consisted of a 725- μm -thick undoped $\langle 100 \rangle$ Si substrate, a 2- μm -thick SiO_2 middle layer, and a 500-nm-thick crystalline-silicon (c-Si) top layer. A negative resist (HSQ FOX16) was coated directly onto the c-Si at 3000 RPM for 60 seconds and baked on a hotplate at 90°C for 5 minutes. The pattern was exposed by using an electron-beam lithography system (EBPG5000Plus, Raith) operated at 100 kV. The resist was developed with tetramethylammonium hydroxide and the pattern transfer was realized by using an inductively coupled plasma tool (Oxford Instruments). The procedure for fabricating the metasurfaces is schematically illustrated in Figure S12.

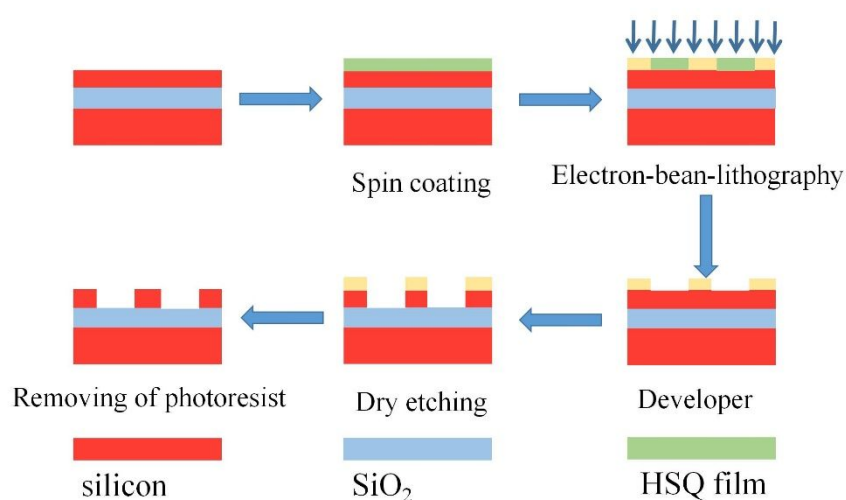


Figure S12. Flow chart for the fabrication of metasurface composed of Si cuboids with and without defects.

Supplementary Note 17: SEM images of the fabricated metasurfaces

In our experiments, we fabricated metasurfaces with different structural parameters by using the combination of electron beam lithography and reactive ion etching. The morphologies of the fabricated samples were examined by using scanning electron microscopy (SEM) observations. In Figure S13, we show the SEM images for the metasurfaces composed of Si cuboids with defects.

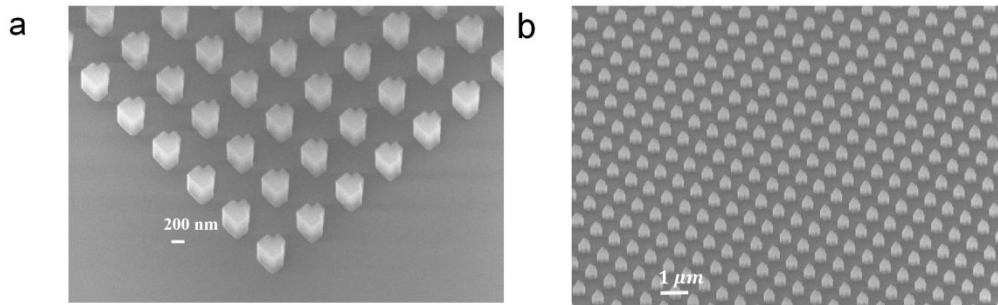


Figure S13. SEM images for the metasurfaces composed of Si cuboids with defects.

References

(1) He, Y.; Guo, G.; Feng, T.; Xu, Y.; Miroshnichenko, A. E. Toroidal Dipole Bound States in the Continuum. *Phys. Rev. B* **2018**, *98*, 161112.